

Full paper

## A self-powered 3D activity inertial sensor using hybrid sensing mechanisms

Kah How Koh<sup>a,\*</sup>, Qiongfeng Shi<sup>b,c,d</sup>, Sen Cao<sup>a</sup>, Daiqun Ma<sup>a</sup>, Hou Yang Tan<sup>a</sup>, Zhenwei Guo<sup>a</sup>, Chengkuo Lee<sup>b,c,d,\*\*</sup>

<sup>a</sup> School of Engineering, Republic Polytechnic, 9 Woodlands Avenue 9, Singapore 738964, Singapore

<sup>b</sup> Department of Electrical and Computer Engineering, National University of Singapore, 4 Engineering Drive 3, Singapore 117576, Singapore

<sup>c</sup> Center for Intelligent Sensors and MEMS, National University of Singapore, 5 Engineering Drive 1, Singapore 117608, Singapore

<sup>d</sup> Hybrid-Integrated Flexible (Stretchable) Electronics Systems Program, National University of Singapore, 5 Engineering Drive 1, Singapore 117608, Singapore

### ARTICLE INFO

#### Keywords:

Self-powered  
Energy harvesting  
Inertial sensor  
Hybrid mechanism  
Healthcare monitoring

### ABSTRACT

A self-powered 3D activity inertial sensor (3DAIS) is proposed for multi-axis acceleration and rotation inertial sensing. The 3DAIS consists of magnetic buckyballs encapsulated inside a 3D-printed spherical shell, with multi-layers of PTFE, PVDF and Al films fabricated on the inner walls of the shell and wire coils wound on the outside. The device demonstrated good performance in hand motion recognition and human activity state monitoring application. When operating as a 6-axis inertial sensor, the 3DAIS is able to sense X, Y and Z-acceleration during linear motion as well as detect roll, pitch and yaw angular velocity during rotational motion. The device possesses self-powering ability as well and is able to harvest energy through hybrid mechanisms of piezoelectric, electromagnetic and triboelectric from various energy sources such as 3D vibration, rotation and human motion, etc. The proposed 3DAIS can potentially pave the way to an advance motion sensing system with self-powering capability for wearables and healthcare telemedicine applications.

### 1. Introduction

Today, the field of telemedicine is changing drastically than ever before since its inception. As technology advances at exponential level, so does the widespread affordability and accessibility to basic telemedicine tools. Originally created to treat patients located in remote places, telemedicine is increasingly becoming a tool for convenient medical care [1]. With the rise of telemedicine, the field of mobile health starts to grow as well, with patients starting to use a wide variety of mobile health apps and mobile medical devices that are able to monitor and sense the health status of themselves for disease prevention and treatment. Home-use medical devices that can sense physiological signs and biochemical parameters such as blood pressure, eyeball motion and brain activity, allow patients to gather needed medical information for a doctor's diagnosis, without going into a clinic or hospital [2–6]. Recently, the rapid development of wearable and implantable devices in flexible electronics provides great opportunity to achieve telemedicine by providing more convenient monitoring and diagnosis [7–11]. Among the various dimensions of healthcare monitoring, information on patients' body motion is an indispensable aspect as useful and timely data on their physical state can be obtained for

rehabilitation or diagnostic purposes [12–20]. For example, detection of activity pattern like resting, sitting, walking can be beneficial for elderly health or patients recuperating from rehabilitation.

One of the most common motion monitoring systems currently available is based on an inertial sensor module consisting of multi-axis microelectromechanical systems (MEMS) gyroscope and accelerometer [21–23]. However, these MEMS inertial sensors require external power and limits the energy durability of a mobile motion monitoring system. To overcome this issue, self-powered accelerometers have been investigated for self-sustained sensors in battery-less applications such as healthcare, Internet-of-Things (IoT) and harsh environment monitoring [24–34]. For example, a self-powered kinematic vector sensor developed by Jing et al. derives its operational energy from close proximity triboelectrification of two surfaces fabricated using highly pliable organic films [24]. In another instance, Chen et al. designed a self-powered motion tracking system consisting of an array of triboelectric nanogenerators (TENG) that are able to monitor moving speed, direction, acceleration and position [25]. A symmetrical device design is another popular configuration adopted by the research community for inertial sensing. This include a spherical-shaped TENG consisting of an outer transparent shell and an inner polyfluoroalkoxy ball demonstrated by

\* Corresponding author.

\*\* Corresponding author at: Department of Electrical and Computer Engineering, National University of Singapore, 4 Engineering Drive 3, Singapore 117576, Singapore.

E-mail addresses: [koh\\_kah\\_how@rp.edu.sg](mailto:koh_kah_how@rp.edu.sg) (K.H. Koh), [elelc@nus.edu.sg](mailto:elelc@nus.edu.sg) (C. Lee).

<https://doi.org/10.1016/j.nanoen.2018.11.075>

Received 2 October 2018; Received in revised form 15 November 2018; Accepted 26 November 2018

Available online 29 November 2018

2211-2855/ © 2018 Elsevier Ltd. All rights reserved.

Zhang et al. for accelerometer purpose [26]. However, only single axis acceleration measurement data was shown.

In order to make the sensor even more versatile and able to sense inputs from multiple axes, a 3D acceleration sensor was explored by Pang et al., where three TENGs were integrated together along the x, y and z directions [31]. However, such design greatly increases the device size and complexity. To overcome this limitation, Shi et al. demonstrated the use of a spherical triboelectric ball for multi-axis acceleration and rotation sensing, and it was the first reported attempt for a self-powered single-axis gyroscope [35]. These spherical designs have also been explored in energy harvesters to harness blue energy from the ocean [36–40]. To further enhance the power of these self-sustaining sensors, different kinds of energy harvesting mechanisms can be integrated in a single device. Such hybrid energy harvesting mechanisms have been widely demonstrated for energy harvesters, tilt sensors and pressure sensors previously [41–55], but this was not the case for multi-axis inertial sensor integrated with self-powering capability. Herein, a self-powered 3D activity inertial sensor (3DAIS), integrated with electromagnetic, piezoelectric and triboelectric hybrid energy harvesting mechanisms, is proposed for 6-axis inertial sensing. The device demonstrates good performance in hand motion recognition and human activity state monitoring application as well as the ability to harvest energy from various external sources such as vibration, rotation and human motion. In general, such self-powered sensing design or dual-purpose design with energy harvesting and sensing capability is a promising research area that can enable advanced motion monitoring systems with long energy durability for applications in the field of wearables and telemedicine.

## 2. Design and operating mechanisms

A schematic drawing of the proposed 3DAIS is shown in Fig. 1(a). The device consists of a 3D printed spherical shell and multi-layers of tape, aluminum (Al), Polyvinylidene Fluoride (PVDF) and Polytetrafluoroethylene (PTFE) films fabricated on the inner wall of the shell. The magnetic buckyball, which is encapsulated inside the shell, is free to move about when the 3DAIS experiences a motion. An enlarged view of the layer-by-layer structure is illustrated in the inset of Fig. 1(a). The Al films function as electrodes for external wire connections, while the piezoelectric PVDF film is sandwiched between the electrodes to form a capacitive structure. The layer of tape in between the shell and the Al electrode serves as cushion and allows the PVDF film to be deformed more in the presence of a mass, thus enhancing the piezoelectric energy harvesting capability. The PTFE film, which is in contact with the magnetic buckyball, will contribute to triboelectrification effect when the magnetic buckyball mass moves inside the sphere. Besides triboelectric energy harvesting, the movement of the magnetic mass will also generate energy by electromagnetic induction in the wire coils wound on the exterior of the shell. Therefore, the 3DAIS is able to generate electrical output simultaneously from the piezoelectric PVDF film, triboelectric surfaces and electromagnetic coils in the presence of mechanical motion in the environment.

Fig. 1(b) shows the outer view photograph of the 3DAIS. Openings were made in the spherical shell so as to allow conducting wires from the Al electrodes to be connected to external equipment for characterization. To form the EM coils, enameled copper wires were wound around each half of the spherical shell. Fig. 1(c) shows the inner view photograph of the device, with the multi-layers of cushion tape, PVDF film with top and bottom Al electrodes, insulating tape and PTFE film with Al electrode fabricated on the inner walls of the shell. The PVDF and PTFE films are cut into leaf shapes, instead of a hemispherical one, so that a flat layer can be formed on the walls. The magnetic buckyballs are then magnetized together in a flat hexagonal shape and encapsulated in the 3DAIS. Table 1 summarizes the dimensions for the different material used in the device.

Due to the 3D symmetrical and spherical design, the device has the

ability to harness energy from diversified multi-dimensional external sources and this translates to a potential for complex and advance motion sensing. Although complex motion may exhibit random direction movement and rotation, it can always be considered as an integration of linear movement in X, Y, Z axes and rotation. Accordingly, the movement of the magnetic buckyballs inside the 3DAIS can also be categorized into in-plane horizontal motion along the X and Y axes, out-of-plane vertical motion along the Z-axis and rotation along the inner walls of the sphere. Fig. 2 shows the electromagnetic energy harvesting mechanism when the 3DAIS is subjected to an in-plane motion, with a magnetic buckyball being considered for illustration purpose. There are two sets of electromagnetic coils, left and right, fabricated on the exterior wall of the sphere. Conducting wires are connected to the ends of both sets of coils for characterization purpose. When the 3DAIS encounters a linear periodic movement along the X-axis, there will be a change in magnetic flux density going through both sets of coils as the magnetic buckyball moves, resulting in electromagnetic induction and electromotive forces  $V_{EML}$  and  $V_{EMR}$  to be generated across the left and right coil, respectively. Similar phenomenon will be observed when the device moves or rotates along the different axes.

Fig. 3 depicts the piezoelectric energy harvesting mechanism when the 3DAIS is subjected to vibration in the x-axis. Similar to the electromagnetic coils, there are two sets of piezoelectric film stack, left and right, which are mechanically and electrically isolated from each other. Conducting wires are connected to the top and bottom electrodes of both film stacks for electrical readout. When the 3DAIS encounters a linear periodic movement along the x-axis, the magnetic buckyballs will oscillate as well, deforming the film stacks and generating  $d_{33}$  piezoelectric voltage  $V_{PEL}$  and  $V_{PER}$  across the left and right PVDF film, respectively. This energy harvesting mechanism is applicable for linear movement in the Y, Z axes and rotation movement as well.

For triboelectric energy harvesting, there are four Al electrodes with conducting wires attached to them, and the harvesting mechanism illustrated in Fig. 4. When the magnetic buckyballs come into contact with the PTFE film, the buckyballs become positively charged while the PTFE becomes negatively charged due to their material difference in electron affinity. When the buckyballs move to the left side, an electrical potential difference  $V_{TE1}$  appears on the two opposite electrodes, which drives electrons flow from the left electrode to the right electrode until a new balance is achieved. When the buckyballs move from the left side to the middle and then further to the right side, electrons flow will be in the opposite direction instead, generating an electrical potential difference of  $V_{TE2}$ . When the 3DAIS is vibrating solely along x or y-axis, there will only be one output in the corresponding direction since there is no electrical potential difference in the other direction. However, when the device is vibrating with a certain angle with respect to the axes, there will be two simultaneous outputs from  $V_{TE1}$  and  $V_{TE2}$ . Thus the device is able to harvest energy from in-plane vibration source in random and multiple directions.

## 3. Results and discussion

### 3.1. Experimental setup

In order to characterize the electrical outputs of the 3DAIS, the conducting wires are first connected to a Keithley 6514 System Electrometer and then subsequently connected to an Agilent Digital Oscilloscope DSO-X-3034A as shown in Fig. 5(a). The electrometer allows for precise low current measurements while the digital oscilloscope displays the waveforms of the electrical current and voltage outputs. Commercial accelerometer ADXL335 and gyroscope ADXRS622, which measure the actual magnitude of the linear acceleration and angular rotation respectively, were mounted on the device during the experiments. DC power supply E3631A from Agilent Technologies is used to power up the commercial accelerator and gyroscope.

After the fabrication of the multi-layers of films and electrodes,

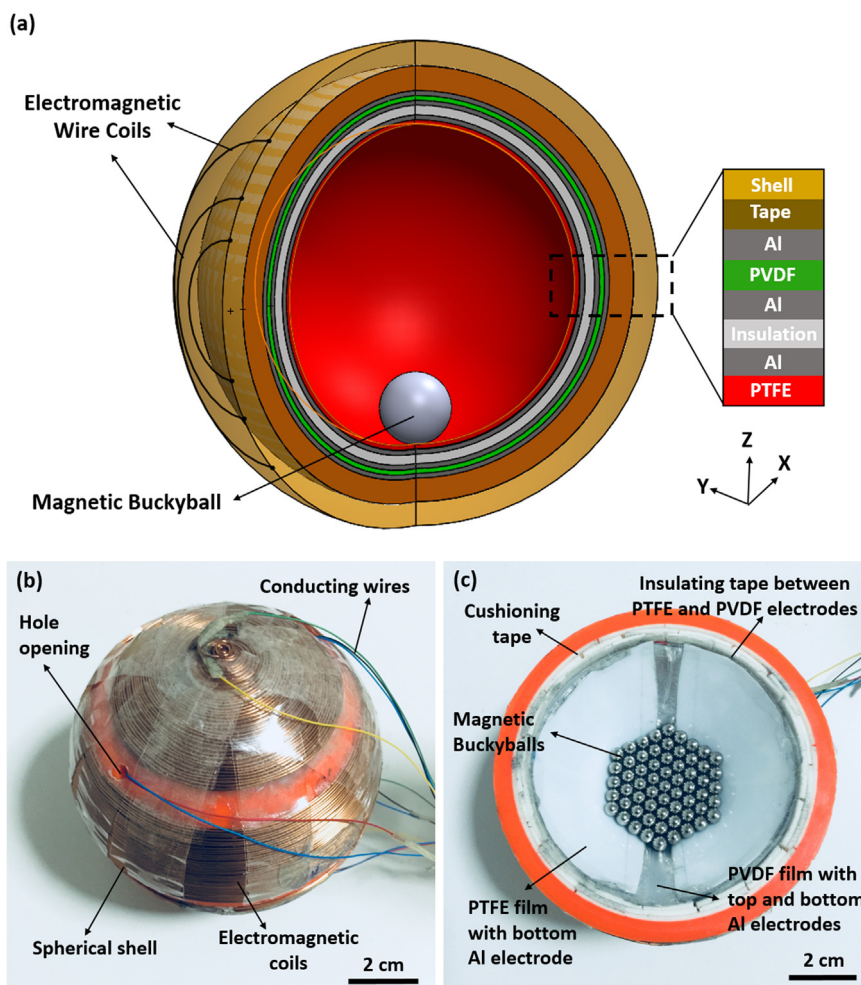


Fig. 1. (a) Schematic drawing of the proposed 3DAIS. Only one buckyball is drawn for illustration purpose. Photographs showing the (b) outer view and (c) inner view of the device.

Table 1  
Dimensions of the material used in the 3DAIS.

Parameter	Value
Outer radius of spherical shell	5 cm
Inner radius of spherical shell	4.5 cm
Thickness of cushion tape	0.5 cm
Thickness of PVDF film	200 $\mu\text{m}$
Thickness of insulation film	0.5 cm
Thickness of PTFE film	100 $\mu\text{m}$
No of EM coils on each half of the shell	180
Diameter of magnetic buckyball	5 mm

multiple buckyballs functioning as movable magnetic mass and triboelectric surface are put inside the spherical shell as shown in Fig. 5(b). Fig. 5(c) illustrates the different number of magnetic buckyballs (19, 37, 61, 91, 127) arranged in a hexagonal shape being investigated. The number of magnetic buckyballs is a key parameter that is expected to have considerable impact on the output performance for all the three energy harvesting mechanisms. For the experiments conducted in Section 3.2, the 3DAIS is periodically vibrated along the x-axis and with a displacement amplitude of 26 cm as depicted in Fig. 5(d). In addition, the non-contact surface area of the buckyballs are taped together with a flexible organic film so that the buckyballs remain in a flat state throughout the vibration motion.

### 3.2. Energy harvesting characterization

The schematic illustration of the electromagnetic energy harvesting is shown in Fig. 6(a) while the output voltages  $V_{EMR}$ ,  $V_{EML}$  and currents  $I_{EMR}$ ,  $I_{EML}$  obtained from the electromagnetic coils are measured and plotted in Fig. 6(b) for different numbers of magnetic buckyballs. It can be observed that the average peak voltages  $V_{EML}$ ,  $V_{EMR}$  and currents  $I_{EML}$  and  $I_{EMR}$  first increase with increasing number of magnetic buckyballs, peaking at 91 buckyballs with  $V_{EML}$ ,  $V_{EMR}$ ,  $I_{EML}$ ,  $I_{EMR}$  having average peak values of 8.6 mV, 10.8 mV, 40.0  $\mu\text{A}$ , 37.5  $\mu\text{A}$ , respectively. With increase number of buckyballs, the magnetic field strength of the movable mass increases as well, resulting in larger voltages and currents generated by electromagnetic induction. However, both the voltage and current outputs decrease subsequently when 127 buckyballs are used. This is due to the movable mass becoming too bulky when it increases further to 127 buckyballs and is unable to conform to the spherical contour of the device, thus resulting in the movement of the mass to become slower. This leads to decrease rate of change of magnetic flux density, causing the induced voltages and currents to drop as well. Even though the device is highly symmetrical, there is still disparity noted between the electrical outputs of the left and right coils. This is due to the fabrication imperfection while winding both sets of coils on the exterior of the shell. Fig. 6(c)–(f) show examples of the output current and voltage waveforms from the two coils when 127 magnetic buckyballs vibrate along the x-axis. The maximum peak currents for the left and right coil are 33  $\mu\text{A}$  and 22  $\mu\text{A}$ , respectively while the maximum peak voltages for the left and right coil are 13 mV and

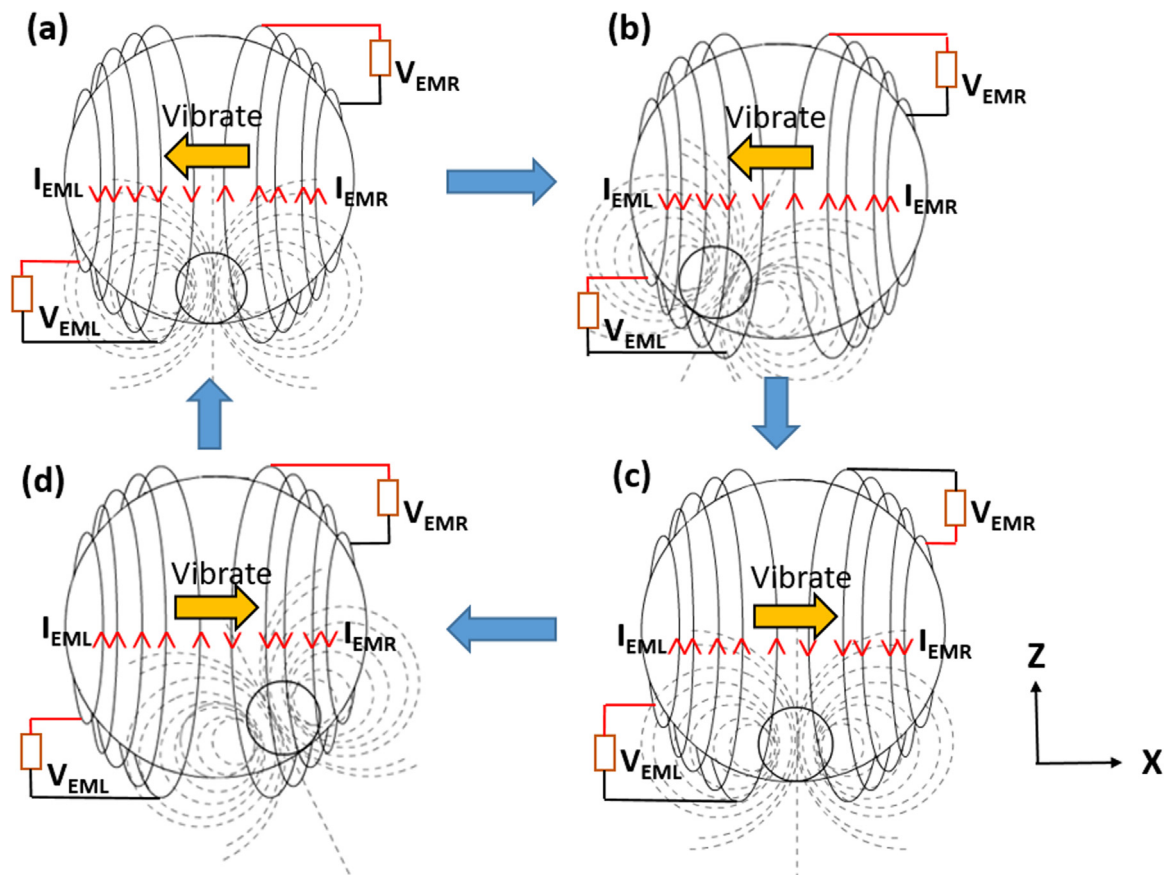


Fig. 2. Schematic diagram illustrating the side view of the electromagnetic energy harvesting mechanism where the magnetic buckyballs are (a) at equilibrium position, (b) moving to the left, (c) back to equilibrium position, and (d) moving to the right when subjected to an in-plane vibration.

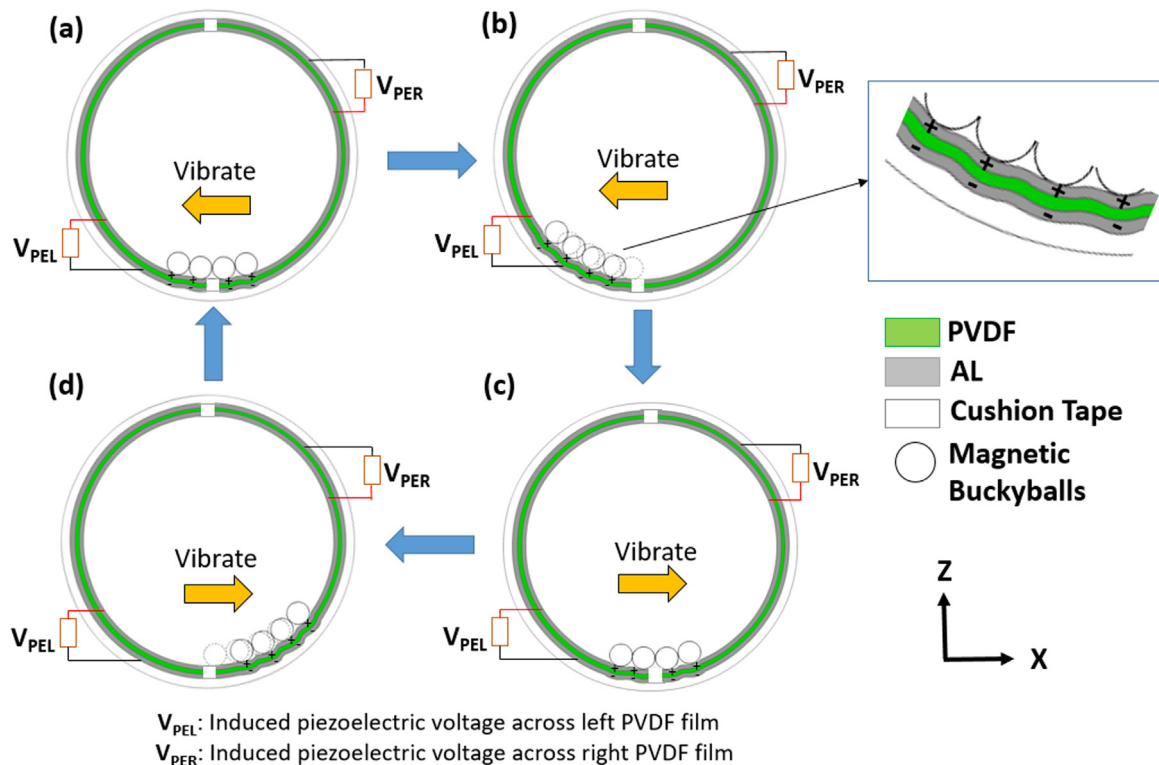


Fig. 3. Schematic diagram illustrating the side view of the piezoelectric energy harvesting mechanism where the magnetic buckyballs are (a) at equilibrium position, (b) moving to the left, (c) back to equilibrium position and (d) moving to the right.

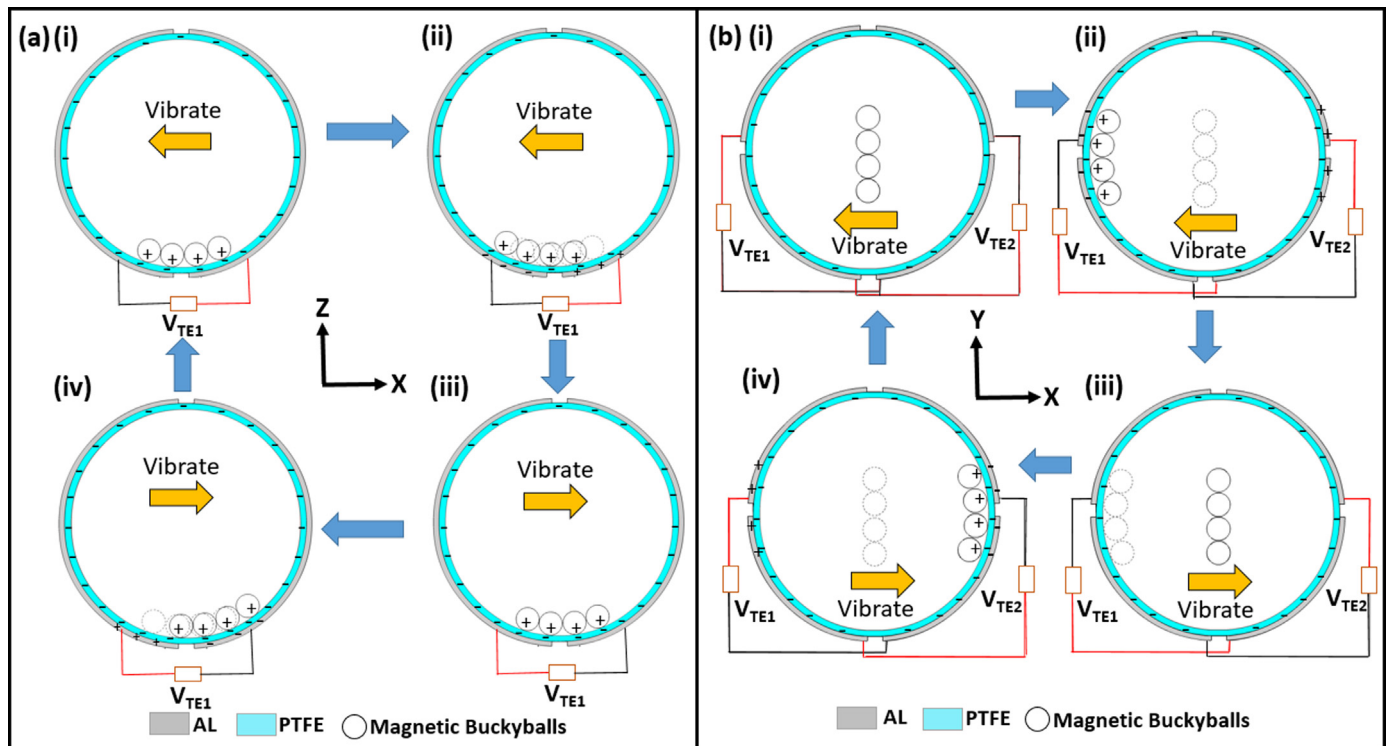


Fig. 4. Schematic diagram illustrating the (a) side view and (b) top view of the triboelectric energy harvesting mechanism.

14 mV, respectively, at an estimated oscillating frequency of 2.5 Hz.

Similar experiments were performed for the piezoelectric energy harvesting portion, with the schematic diagram illustrating the characterization depicted in Fig. 7(a). The output voltages  $V_{PEL}$ ,  $V_{PER}$  and currents  $I_{PEL}$ ,  $I_{PER}$  obtained from the left and right piezoelectric film stacks are measured and plotted in Fig. 7(b) for varying numbers of magnetic buckyballs. Unlike the trend observed for electromagnetic energy harvesting, the average peak voltages  $V_{PEL}$ ,  $V_{PER}$  and currents  $I_{PEL}$ ,  $I_{PER}$  increase with increasing number of magnetic buckyballs for piezoelectric energy harvesting. At 127 magnetic buckyballs, the average peak voltages  $V_{PEL}$ ,  $V_{PER}$  and current  $I_{PEL}$ ,  $I_{PER}$  obtained are 1.2 V, 1.7 V, 116 nA and 132 nA, respectively. With greater number of magnetic buckyballs, the weight exerted by the movable mass on the piezoelectric film stacks increases, resulting in greater film deformation and electrical outputs. In addition, the average peak current observed for piezoelectric energy harvesting is two orders of magnitude smaller than that obtained for electromagnetic energy harvesting. This is due to the piezoelectric film stack being a capacitive structure, thus having a higher impedance compared with the resistive electromagnetic coils. Illustrations of the output voltage and current waveforms, at approximately 2.5 Hz frequency, obtained from both sets of piezoelectric film stacks are shown in Fig. 7(c)–(f).

Fig. 8 depicts the results derived from triboelectric energy harvesting characterization. Similar to piezoelectric energy harvesting, the triboelectric electrical output increases with increasing number of buckyballs, reaching values of 3.7 V, 5.7 V, 91 nA, 150 nA for  $V_{TE1}$ ,  $V_{TE2}$ ,  $I_{TE1}$  and  $I_{TE2}$ , respectively, when 127 magnetic buckyballs were used. This is expected as the contact area between the hexagonal movable mass and the PTFE film increases with greater number of buckyball balls, resulting in greater contact electrification. Waveform plots of the output voltage and current obtained from both sets of PTFE films are shown in Fig. 8(c)–(f) at approximately 3 Hz vibration frequency. Among the three energy harvesting mechanisms, the electromagnetic coils produce the largest current in the microampere range, while the triboelectric PTFE films generate the largest voltage output.

The load characteristics of the 3DAIS are measured for

electromagnetic, piezoelectric and triboelectric mechanisms and shown in Fig. 9(a), (b) and (c), respectively. Load resistance varying from 0  $\Omega$  to 20 M $\Omega$  are used to obtain the corresponding peak average current and voltages, while the peak power values are calculated using  $I_{load}^2 R_{load}$  or  $V_{load}^2 / R_{load}$ . As shown in Fig. 9(a), the instantaneous power output  $P_{EML}$ ,  $P_{EMR}$  of the left and right electromagnetic coils reach a maximum value of 13.8 nW and 22.4 nW, at an optimized load impedance of 25  $\Omega$  and 20  $\Omega$ , respectively. In the case of piezoelectric energy harvesting in Fig. 9(b), the maximum output power  $P_{PEL}$ ,  $P_{PER}$  for the left and right piezoelectric PVDF films are 0.12  $\mu$ W and 0.19  $\mu$ W, obtained at load impedance of 10 M $\Omega$ , respectively. Similarly for triboelectric energy harvesting, the peak power  $P_{TE1}$ ,  $P_{TE2}$  generated for the 1st and 2nd set of PTFE films are 0.22  $\mu$ W and 0.72  $\mu$ W, which are attained at optimum load impedance of 12 M $\Omega$  and 15 M $\Omega$ , respectively. In terms of power spectrum, the triboelectric PTFE films generate the largest loaded power, followed by piezoelectric PVDF films and finally electromagnetic coils.

### 3.3. Self-powered advanced motion sensor

Apart from the three-dimensional energy harvesting capability, the 3DAIS is ideally suitable for self-powered advanced motion sensing applications as well. Unlike commercially available accelerometer and gyroscope which require supply of power to work, the proposed 3DAIS is inherently self-sustaining and this removes the need for an external energy source. In addition, the proposed 3DAIS is able to sense linear and rotation motions in multiple axes, compared to conventional energy harvesters which can only achieve single axis sensing.

As shown in Fig. 10(a), acceleration of different magnitudes are applied on the device at a fixed frequency of 3 Hz along x, y and z-axis, using triboelectric voltage  $V_{TE2}$ , electromagnetic current  $I_{EMR}$  and piezoelectric voltage  $V_{PER}$  to sense the different linear motions, respectively. Triboelectric voltage is used for x-acceleration sensing output as the voltage output from triboelectric energy harvesting is the largest, evident from previous experiment. Piezoelectric voltage, on the other hand, is used to sense z-acceleration as the impact from the magnetic

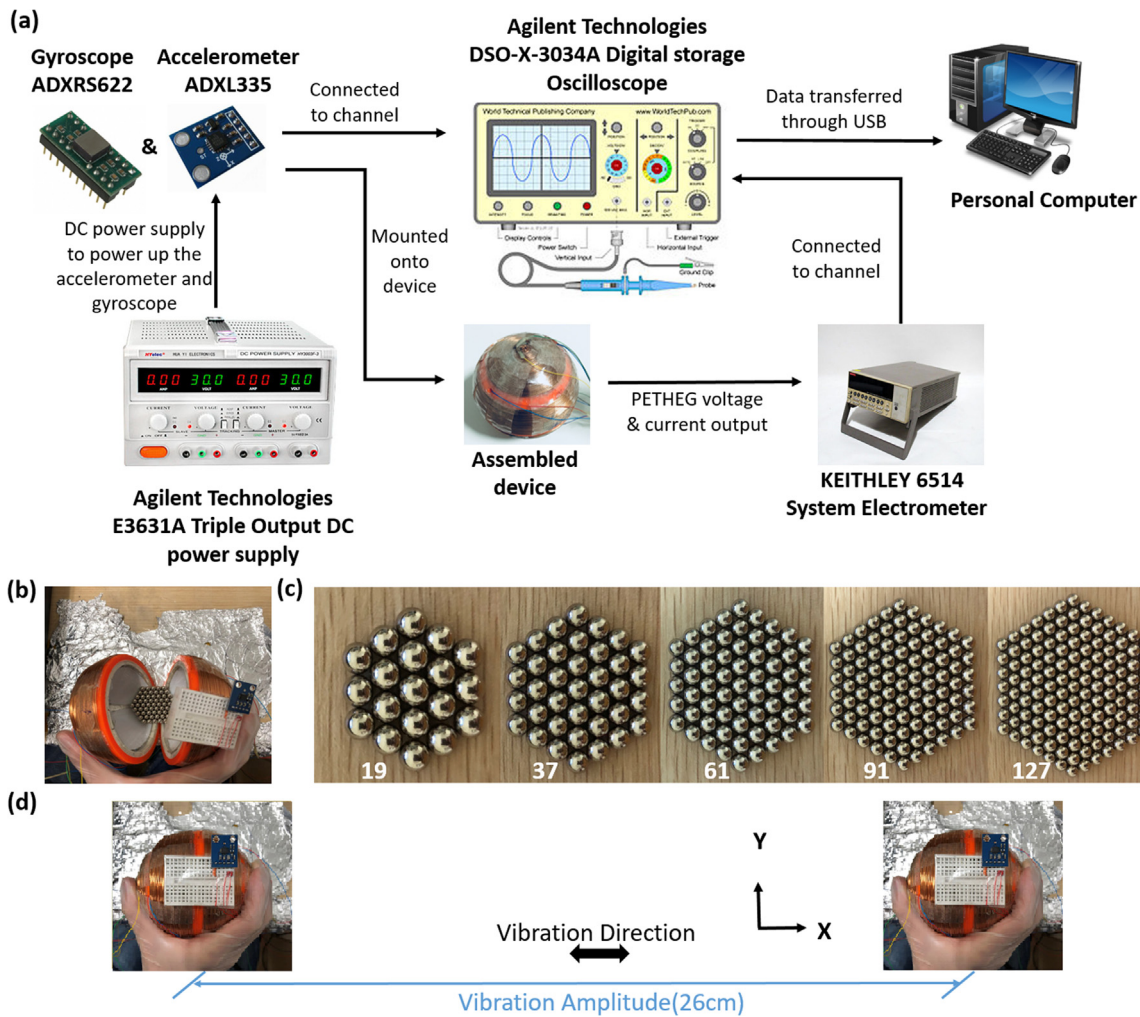


Fig. 5. (a) Experimental setup to characterize the various energy harvesting mechanisms of the 3DAIS. Photos illustrating the (b) initial position of the magnetic buckyballs, (c) configuration and number of magnetic buckyballs used during characterization. (d) Schematic diagram showing the vibration amplitude and direction when performing characterization along x-axis.

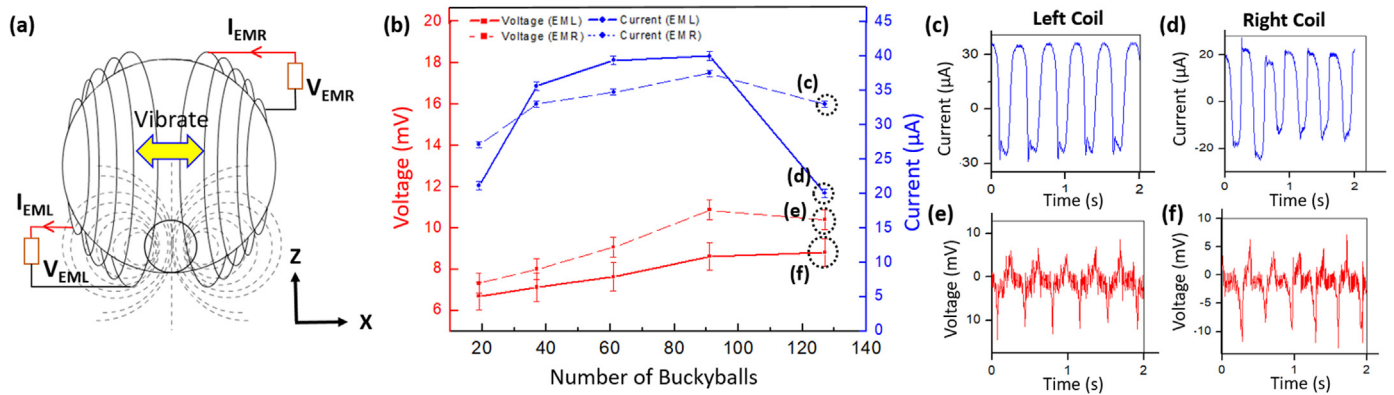


Fig. 6. (a) Schematic diagram illustrating the electromagnetic energy harvesting characterization along the x-axis. (b) Peak output voltages  $V_{EML}$ ,  $V_{EMR}$  and currents  $I_{EML}$ ,  $I_{EMR}$  as a function of number of magnetic buckyballs obtained from the left and right coils. (c)–(f) Peak output current and voltage waveforms generated from the left and right coils, respectively, when 127 magnetic buckyballs vibrate along the x-axis.

buckyballs dropping on the PVDF film in z-direction is expected to be the biggest compared to magnetic buckyballs rolling on the PVDF film in x or y-direction. For acceleration sensing in y-direction, current output from the coils, instead of voltage, is chosen as the current output from electromagnetic energy harvesting is the largest among the three mechanisms. With this sensing configuration, the device is able to sense

and provide readout simultaneously for the 3 acceleration axes. Fig. 10(b) illustrates the 3DAIS being used for self-powered hand motion recognition application, where the device is held by a human hand. A commercial 3-axis accelerometer ADXL335 is assembled on a breadboard and mounted on top of the device for actual acceleration measurement. Output voltages and current from triboelectric,

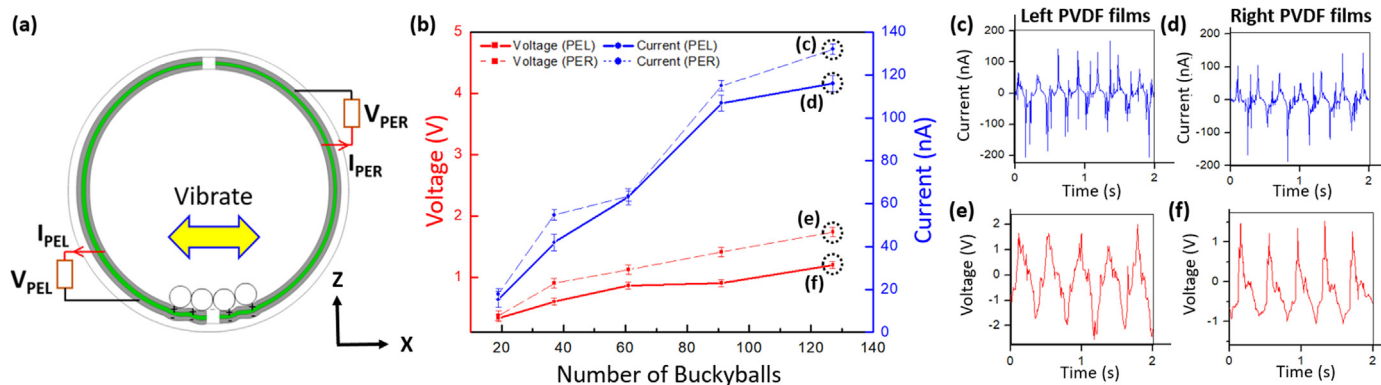


Fig. 7. (a) Schematic diagram illustrating piezoelectric energy harvesting characterization along the x-axis. (b) Peak output voltages  $V_{PEL}$ ,  $V_{PER}$  and currents  $I_{PEL}$ ,  $I_{PER}$  as a function of number of buckyballs obtained from the left and right PVDF films. (c)–(f) Peak output voltage and current waveforms generated from the left and right PVDF films, respectively, when 127 magnetic buckyballs vibrate along the x-axis.

electromagnetic and piezoelectric mechanisms are connected to the different channels of the oscilloscope for waveform recording when the device moves left and right along x-axis, front and back along y-axis, up and down along z-axis.

Fig. 10(c) presents the relationship of triboelectric, piezoelectric voltages with x, z-acceleration and electromagnetic current with y-acceleration, respectively, when 91 magnetic buckyballs are encapsulated and oscillating inside the sphere. The electrical outputs increase with increasing acceleration for all the three axis. This is because during in-plane sliding mode, the rate of change of relative displacement between the movable mass and the triboelectric films becomes greater with increasing x-acceleration, resulting in bigger dipole polarization and potential difference  $V_{TE2}$  generated across the two electrodes. Similarly, when the y-acceleration increases, the magnetic buckyballs moves faster, causing the rate of change of magnetic flux density of it relative to the external coils to increase as well, resulting in higher electromagnetic current  $I_{EMR}$ . In the case of z-axis, the resultant force acting on the magnetic mass becomes bigger with increasing z-acceleration, ensuring a greater deformation on the piezoelectric film and voltage output  $V_{PER}$ . For x-acceleration sensing, there are two different sensing range 1 g to 1.75 g and 1.75 g to 3 g, with a sensitivity of  $3.88 \text{ V g}^{-1}$  and  $0.75 \text{ V g}^{-1}$ , respectively. In the case for y-acceleration sensing, the two sensing ranges are 1 g to 2.25 g and 2.25 g to 3 g, with sensitivity of  $6.55 \mu\text{A g}^{-1}$  and  $48.87 \mu\text{A g}^{-1}$ . Finally, for z-acceleration sensing, the sensitivity is uniform at  $0.79 \text{ V g}^{-1}$  over a sensing range of 1 g to 3 g. Fig. 10(d) shows the waveforms of the acceleration from the commercial accelerometer and electrical outputs from the three mechanisms when the device moves to left and right along x-axis, front and back

along y-axis, up and down along z-axis in a periodic motion. When the device moves to the left, x-acceleration and  $V_{TE2}$  show onset of peaks simultaneously. Meanwhile, there are no signals recorded from y and z-acceleration as the characterization is performed along x-axis only. As expected, there are also no significant signals recorded from  $V_{EMR}$  and  $V_{PER}$  as triboelectric voltage generation dominates among the three mechanisms when vibrating along the x-axis. Similarly, when the device moves to the right, x-acceleration and  $V_{TE2}$  show several vibrating peaks, while no signals are observed for  $V_{EMR}$ ,  $V_{PER}$ , y and z-acceleration. When moving the device front and back, current, which is being deployed as the electrical sensing output, is detected only from the electromagnetic coils. The peak from  $I_{EMR}$  corresponds with the onset of y-acceleration as well and this phenomenon holds for the up-down motion along z-axis where voltage peaks from  $V_{PER}$  corresponds to the onset of z-acceleration. During the up-down motion, the movable mass encapsulated in the sphere lifts off from the bottom surface of the sphere, stay momentarily in air and eventually falls back down to the bottom of the sphere. As such, minimal voltage is generated from triboelectric mechanism as there is negligible rubbing contact between the movable mass and the PTFE film, while the induced electromagnetic voltage remains in the millivolts range and is insignificant when compared with the piezoelectric voltage generated from the deformation of the PVDF film.

Besides linear acceleration, the 3DAIS is also investigated for rotational motion sensing as well. Fig. 11(a) depicts angular motion being applied on the device at the same fixed frequency of 3 Hz along x, y and z-axis, using triboelectric voltage  $V_{TE1}$  for roll sensing, electromagnetic current  $I_{EML}$  for pitch sensing and piezoelectric voltage  $V_{PEL}$  for yaw

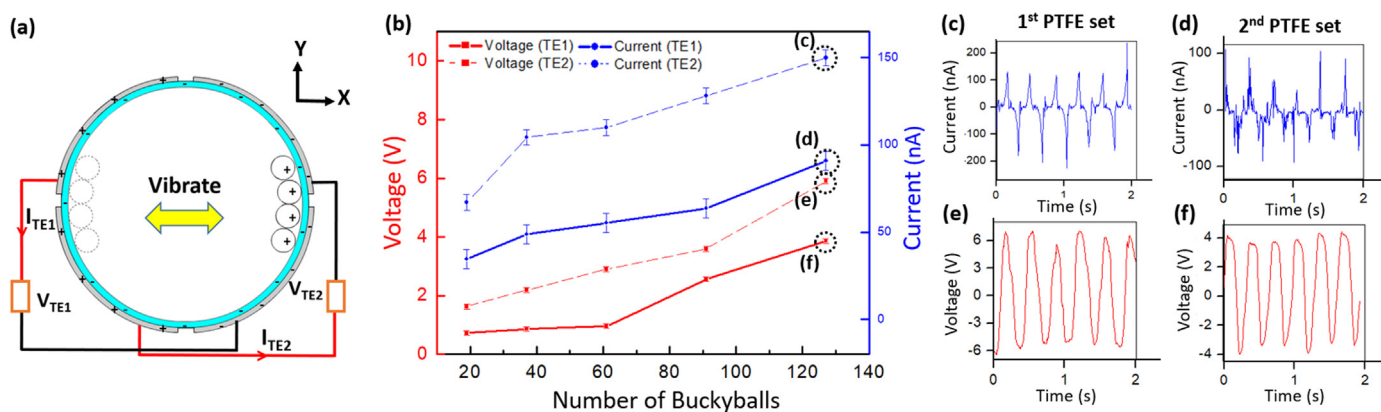


Fig. 8. (a) Schematic diagram illustrating triboelectric energy harvesting characterization along the x-axis. (b) Output voltages  $V_{TE1}$ ,  $V_{TE2}$  and currents  $I_{TE1}$ ,  $I_{TE2}$  as a function of number of buckyballs obtained from the 1st and 2nd set of PTFE films. (c)–(f) Output current and voltage waveforms generated from the 1st and 2nd set of PTFE films, respectively, when 127 buckyballs vibrate along the x-axis.

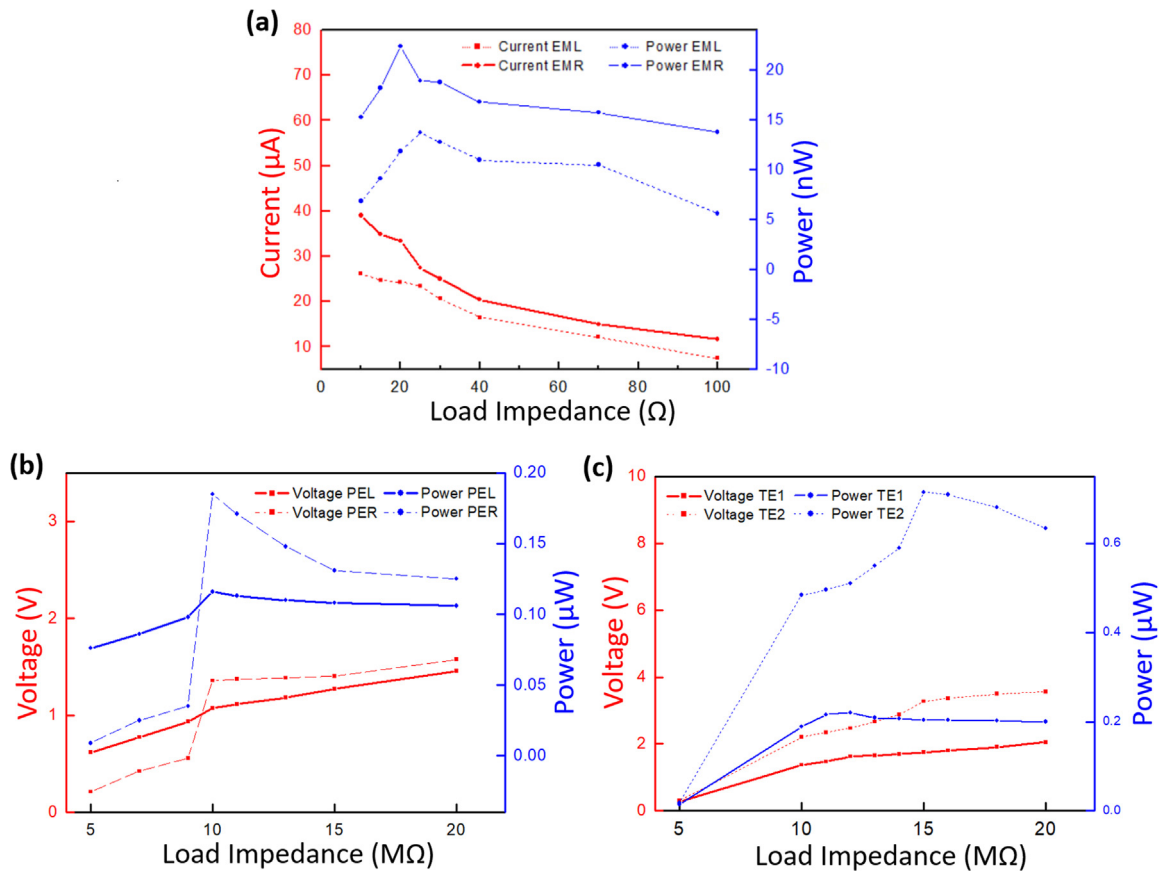


Fig. 9. Peak (a) electromagnetic current, (b) piezoelectric voltage, (c) triboelectric voltage and their peak power characteristic as a function of various load resistances, when 91 magnetic buckyballs vibrate along the x-axis.

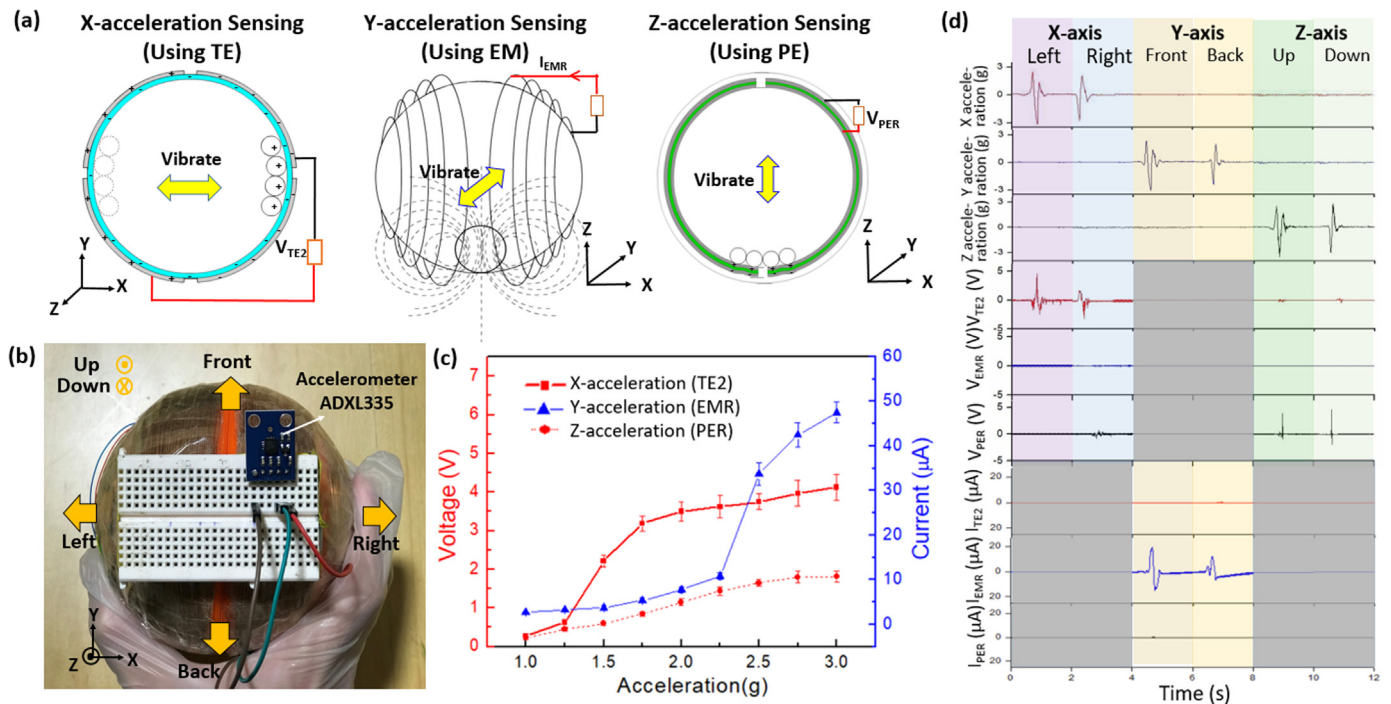
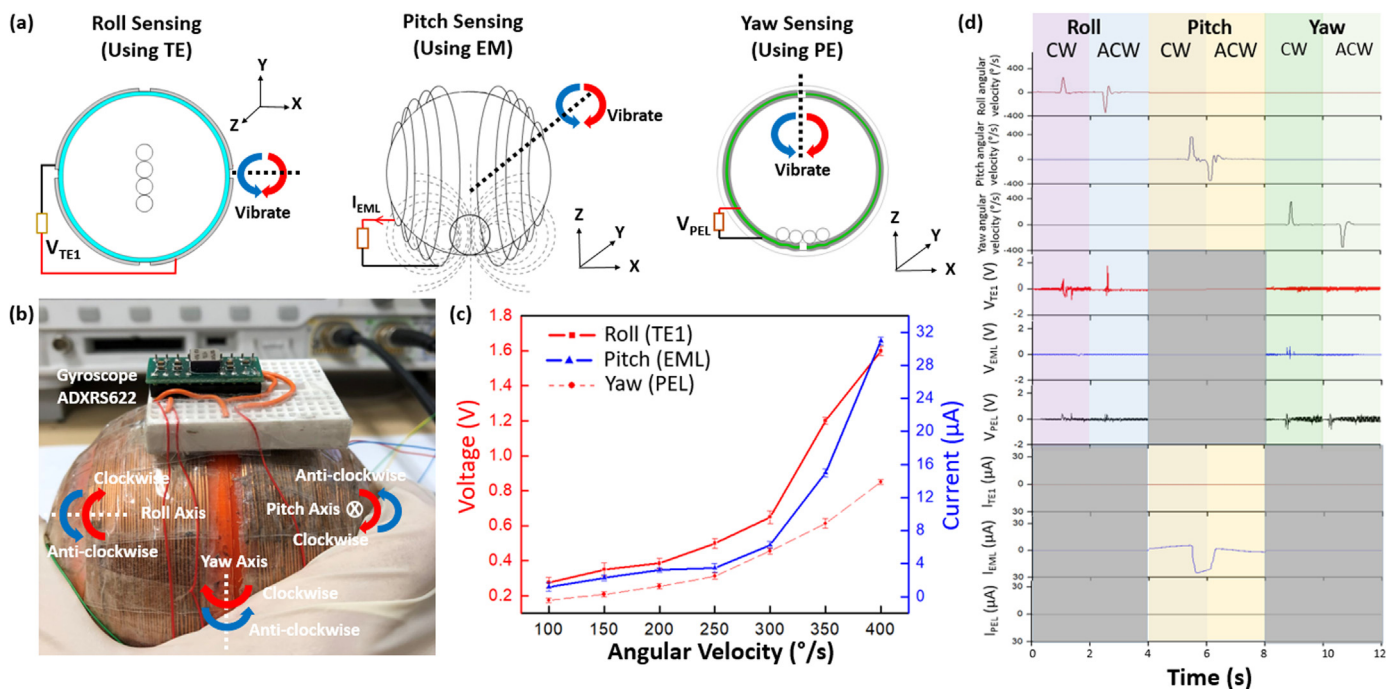


Fig. 10. (a) Schematic diagram illustrating the use of triboelectric output voltage  $V_{\text{TE2}}$  for x-axis acceleration sensing, electromagnetic output current  $I_{\text{EMR}}$  for y-axis acceleration sensing and piezoelectric output voltage  $V_{\text{PER}}$  for z-axis acceleration sensing. (b) Photograph of the 3DAIS, with a 3-axis accelerometer ADXL335 mounted on top of it and the different vibration directions performed during characterization. (c) Voltage and current generated as a function of acceleration for X, Y and Z-acceleration sensing. (d) Acceleration level and the output voltage waveforms from the 3DAIS when it moves left right along X-axis, front back along Y-axis and up down along Z-axis.



**Fig. 11.** (a) Schematic diagram illustrating the use of triboelectric output voltage  $V_{TE1}$  for roll sensing, electromagnetic output current  $I_{EML}$  for pitch sensing and piezoelectric output voltage  $V_{PEL}$  for yaw sensing. (b) Photograph of the 3DAIS, with gyroscope ADXR622 mounted on it during characterization. (c) Voltage and current generated as a function of angular velocity for roll, pitch and yaw sensing. (d) Angular velocity level and the output voltage waveforms from the 3DAIS when it rotates clockwise and anti-clockwise along the roll, pitch and yaw axis.

sensing to sense the different rotation motions, respectively. This configuration is similar to that used for acceleration sensing, except that the electrical signal readouts are from the other set of electrodes. Fig. 11(b) illustrates the 3DAIS being used for self-powered rotating human gesture recognition application, where the device is held by a human hand for rotation sensing. A commercial gyroscope ADXR662 is assembled on a breadboard and mounted on top of the device for actual angular velocity measurement. As the commercial gyroscope is only able to measure yaw angular motion, it will be attached to the device in different orientations in order to meet the characterization requirement. Fig. 11(c) shows the output of roll, pitch and yaw sensing when the angular velocity is varied from  $100\text{ s}^{-1}$  to  $400\text{ s}^{-1}$ , with the rotation angle and number of magnetic buckyballs fixed at  $60^\circ$  and 91, respectively. In the angular velocity range of  $100\text{ s}^{-1}$  to  $300\text{ s}^{-1}$ , the sensitivity for roll, pitch and yaw sensing are  $1.75\text{ mV}(\text{s}^{-1})^{-1}$ ,  $0.03\text{ }\mu\text{A}(\text{s}^{-1})^{-1}$  and  $1.2\text{ mV}(\text{s}^{-1})^{-1}$ , respectively. For the higher angular velocity range of  $300\text{ s}^{-1}$  to  $400\text{ s}^{-1}$ , the sensitivity increases to  $9.8\text{ mV}(\text{s}^{-1})^{-1}$ ,  $0.25\text{ }\mu\text{A}(\text{s}^{-1})^{-1}$  and  $3.8\text{ mV}(\text{s}^{-1})^{-1}$  for roll, pitch and yaw, respectively.

Fig. 11(d) depicts the waveforms of the angular velocity from the commercial gyroscope and electrical outputs from the three mechanisms when the device rotates clockwise (CW) and anti-clockwise (ACW) along the roll, pitch and yaw axes in a periodic motion. Phenomenon observed for angular motion is similar to that for acceleration, with primary outputs observed from triboelectric voltage  $V_{TE1}$ , electromagnetic current  $I_{EMR}$  and piezoelectric voltage  $V_{PER}$  for roll, pitch and yaw angular motion, respectively. When the 3DAIS is subjected to different linear and angular motions, the different output waveforms of  $V_{TE1}$ ,  $V_{TE2}$ ,  $I_{EML}$ ,  $I_{EMR}$ ,  $V_{PEL}$ ,  $V_{PER}$  can be identified by a signal processing circuit and hence able to serve as input signals for a motion recognition system.

To further demonstrate the potential of our self-powered 3DAIS in a healthcare monitoring application, the device is attached to various parts of a human body for supervision of daily activity state or exercise level, which is important for rehabilitation and diagnostics purposes. As shown in Fig. 12(a), the 3DAIS is mounted at the hand, waist and ankle

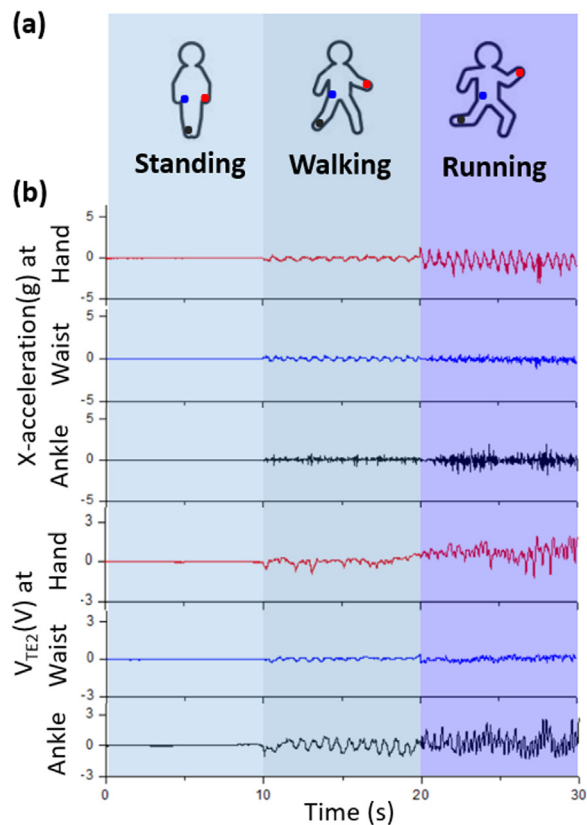


**Fig. 12.** (a) Schematic illustration of the 3 types of exercise states standing, walking and running carried out, with the 3DAIS mounted at the hand (red dot), waist (blue dot) and ankle (black dot) during the activities. (b) The acceleration level and the output triboelectric voltage  $V_{TE2}$  from the 3DAIS when the person is standing, walking and running.

for different exercise state sensing such as standing, walking and running, with the x-direction of the device aligned with the moving direction of the human being. While standing, walking and running, the output voltage  $V_{TE2}$  from the device is plotted in Fig. 12(b) along with the corresponding acceleration level from the commercial accelerometer. As the exercise state transits from standing to walking and eventually running, the acceleration experienced by both the subject and the device increase, resulting in higher output voltage  $V_{TE2}$ . Other than judging from the output voltage waveform, frequency domain analysis can also be performed to determine the type of exercise the subject is undergoing, as the frequency of the waveform increases as the exercise gets more intense. It is also worthwhile to note that for the same exercise, intensity level at different parts of the body might differs. In this case, it can be inferred that the subject moves his ankle more rapidly compared to his hand and waist when he is running. A video demonstration of the 3DAIS mounted on the subject hand as an exercise sensor can be found in the supplementary material. With the proliferation of telemedicine and growing convenience of providing clinical health care service from a distance, the 3DAIS can be further integrated with a WIFI enabled microcontroller such as Arduino Yun Mini, allowing real-time information such as the voltage output of the 3DAIS and the intensity level of his daily activities to be wirelessly uploaded to a cloud platform for offsite monitoring by medical personnel. This enhanced healthcare monitoring system can potentially be made self-sustaining by leveraging the multi-dimensional energy harvesting capability of the 3DAIS to power up the microcontroller.

#### 4. Conclusion

In conclusion, a 3DAIS is proposed for multi-dimensional energy harvesting and inertial sensing for self-powered advance motion sensing applications. The device incorporates a hybrid of electromagnetic, piezoelectric and triboelectric energy harvesting mechanisms and together with its symmetrical design make it highly versatile in harnessing energy from various types of ambient energy sources. In addition, the device can also operate as a 6-axis inertial sensor, detecting linear acceleration along the x, y, z axes and angular velocity along the roll, pitch, yaw axes. When the device is subjected to various linear and angular motions, the different voltage and current output waveforms can be identified by a signal processing circuit and hence able to serve as input signals for a motion recognition system. Last but not least, the 3DAIS is mounted on various parts of human body to further demonstrate the potential of the device in a motion recognition system for healthcare monitoring application. Looking forward, the proposed 3DAIS can be a key component in realizing a self-powered, self-sustaining and advance motion monitoring system.

#### Acknowledgements

This work was supported by grants from the HIFES Seed Funding-2017-01 grant (R-263-501-012-133) "Hybrid Integration of Flexible Power Source and Pressure Sensors" at the National University of Singapore; Agency for Science, Technology and Research (A\*STAR), Singapore and Narodowe Centrum Badań i Rozwoju (NCBR), Poland Joint Grant (R-263-000-C91-305) "Chip-Scale MEMS Micro-Spectrometer for Monitoring Harsh Industrial Gases".

#### Appendix A. Supplementary material

Supplementary data associated with this article can be found in the online version at [doi:10.1016/j.nanoen.2018.11.075](https://doi.org/10.1016/j.nanoen.2018.11.075).

#### References

- [1] D.A. Perednia, A. Allen, *JAMA* 273 (1995) 483.
- [2] G. Ciuti, L. Ricotti, A. Menciassi, P. Dario, *Sensors* 15 (2015) 6441.
- [3] M. Shi, H. Wu, J. Zhang, M. Han, B. Meng, H. Zhang, *Nano Energy* 32 (2017) 479.
- [4] X. Chen, Y. Song, Z. Su, H. Chen, X. Cheng, J. Zhang, M. Han, H. Zhang, *Nano Energy* 38 (2017) 43.
- [5] M.M. Rodgers, V.M. Pai, R.S. Conroy, *IEEE Sens. J.* 15 (2015) 3119.
- [6] Y. Yang, H. Zhang, Z.-H. Lin, Y.S. Zhou, Q. Jing, Y. Su, J. Yang, J. Chen, C. Hu, Z.L. Wang, *ACS Nano* 7 (2013) 9213.
- [7] W. Jiang, H. Li, Z. Liu, Z. Li, J. Tian, B. Shi, Y. Zou, H. Ouyang, C. Zhao, L. Zhao, R. Sun, H. Zhang, Y. Fan, Z.L. Wang, Z. Li, *Adv. Mater.* 30 (2018) 32.
- [8] H. Feng, C. Zhao, P. Tan, R. Liu, X. Chen, Z. Li, *Adv. Healthc. Mater.* 7 (2018) 1701298.
- [9] B. Shi, Z. Li, Y. Fan, *Adv. Mater.* 30 (2018) 44.
- [10] F. Arab Hassani, R.P. Morgan, G.G.L. Gammad, H. Wang, S.C. Yen, N.V. Thakor, C. Lee, *ACS Nano* 12 (2018) 3487.
- [11] W. Hao, H. Wu, D. Hasan, T. He, Q. Shi, C. Lee, *ACS Nano* 11 (2017) 10337.
- [12] S. Patel, H. Park, P. Bonato, L. Chan, M. Rodgers, *J. Neuroeng. Rehabil.* 21 (2012) 1.
- [13] C.-C. Yang, Y.-L. Hsu, *Sensors* 10 (2010) 7772.
- [14] H. Wu, Z. Su, M. Shi, L. Miao, Y. Song, H. Chen, M. Han, H. Zhang, *Adv. Funct. Mater.* 28 (2017) 1.
- [15] J.J. Park, W.J. Hyun, S.C. Mun, Y.T. Park, O.O. Park, *ACS Appl. Mater. Interfaces* 7 (2015) 6317.
- [16] T. Zhou, C. Zhang, C.B. Han, F.R. Fan, W. Tang, Z.L. Wang, *Appl. Mater. Interfaces* 6 (2014) 14695.
- [17] T. Chen, Q. Shi, K. Li, Z. Yang, H. Liu, L. Sun, J.A. Dziuban, C. Lee, *Nanomaterials* 8 (2018) 613.
- [18] L. Chen, Q. Shi, Y. Sun, T. Nguyen, C. Lee, S. Soh, *Adv. Mater.* 1802405 (2018) 1.
- [19] T. Chen, Q. Shi, M. Zhu, T. He, L. Sun, L. Yang, C. Lee, *ACS Nano* (2018), <https://doi.org/10.1021/acsnano.8b06747>.
- [20] J. Chung, H. Yong, H. Moon, V.D. Quang, S. Choi, D. Kim, S. Lee, *Adv. Sci.* (2018) 1801504.
- [21] C.M.N. Brigante, N. Abbate, A. Basile, A.C. Faulisi, S. Sessa, *IEEE Trans. Ind. Electron.* 58 (2011) 3234.
- [22] G. Shi, C.S. Chan, W.J. Li, K.-S. Leung, Y. Zou, Y. Jin, *IEEE Sens. J.* 9 (2009) 495.
- [23] T. Shany, S.J. Redmond, M.R. Narayanan, N.H. Lovel, *IEEE Sens. J.* 12 (2012) 658.
- [24] Q. Jing, Y. Xie, G. Zhu, R.P.S. Han, Z.L. Wang, *Nat. Commun.* 6 (2015) 1.
- [25] M. Chen, X. Li, L. Lin, W. Du, X. Han, J. Zhu, C. Pan, Z.L. Wang, *Adv. Funct. Mater.* 24 (2014) 1.
- [26] H. Zhang, Y. Yang, Y. Su, J. Chen, K. Adams, S. Lee, C. Hu, Z.L. Wang, *Adv. Funct. Mater.* 24 (2014) 1401.
- [27] H. Yu, X. He, W. Ding, Y. Hu, D. Yang, S. Lu, C. Wu, H. Zou, R. Liu, C. Lu, Z.L. Wang, *Adv. Energy Mater.* 7 (2017) 1.
- [28] H. Askari, Z. Saadatnia, E. Asadi, A. Khajepour, M.B. Khamesee, J. Zu, *Nano Energy* 45 (2018) 319.
- [29] J. Zhu, X. Guo, D. Meng, M. Cho, I. Park, R. Huang, W. Song, *J. Mater. Chem. A* 6 (2018) 16548.
- [30] Q. Shi, H. Wang, H. Wu, C. Lee, *Nano Energy* 40 (2017) 203.
- [31] Y.K. Pang, X.H. Li, M.X. Chen, C.B. Han, C. Zhang, Z.L. Wang, *ACS Appl. Mater. Interfaces* 7 (2015) 19076.
- [32] C.B. Han, C. Zhang, X.H. Li, L. Zhang, T. Zhou, W. Hu, Z.L. Wang, *Nano Energy* 9 (2014) 325.
- [33] Y. Yang, G. Zhu, H. Zhang, J. Chen, X. Zhong, Z.-H. Lin, Y. Su, P. Bai, X. Wen, Z.L. Wang, *ACS Nano* 7 (2013) 9461.
- [34] Y. Wu, Y. Hu, Z. Huang, C. Lee, F. Wang, *Sens. Actuators A* 271 (2018) 364.
- [35] Q. Shi, H. Wu, H. Wang, H. Wu, C. Lee, *Adv. Energy Mater.* 7 (2017) 1.
- [36] Y. Hu, J. Yang, Q. Jing, S. Niu, W. Wu, Z.L. Wang, *ACS Nano* 7 (2013) 10424.
- [37] T.X. Xiao, X. Liang, T. Jiang, L. Xu, J.J. Shao, J.H. Nie, Y. Bai, W. Zhong, Z.L. Wang, *Adv. Funct. Mater.* 28 (2018) 1802634.
- [38] W. Yang, J. Chen, Q. Jing, J. Yang, X. Wen, Y. Su, G. Zhu, P. Bai, Z.L. Wang, *Adv. Funct. Mater.* 24 (2014) 4090.
- [39] L. Xu, T. Jiang, P. Lin, J.J. Shao, C. He, W. Zhong, X.Y. Chen, Z.L. Wang, *ACS Nano* 12 (2018) 1849.
- [40] J. Tuan, H. Feng, L. Yan, M. Yu, H. Ouyang, H. Li, W. Jiang, Y. Jin, G. Zhu, Z. Li, Z.L. Wang, *Nano Energy* 36 (2017) 241.
- [41] X. Chen, H. Guo, H. Wu, H. Chen, Y. Song, Z. Su, H. Zhang, *Nano Energy* 49 (2018) 51.
- [42] Y. Bai, H. Jantunen, J. Juuti, *Adv. Mater.* 30 (2018) 1.
- [43] R.K. Gupta, Q. Shi, L. Dhakar, T. Wang, C.H. Heng, C. Lee, *Sci. Rep.* 7 (7) (2017) 1–13.
- [44] B. Yang, C. Lee, W.L. Kee, S.-P. Lim, *J. Micro/Nanolithogr. MEMS MOEMS* 9 (2010) 1.
- [45] Y.J. Sang, X. Huang, H. Liu, P. Jin, *IEEE Trans. Magn.* 48 (2012) 4495.
- [46] M.-K. Seol, J.-W. Han, S.-J. Park, S.-B. Jeon, Y.-K. Choi, *Nano Energy* 23 (2016) 50.
- [47] Y. Eun, D.-S. Kwon, M.-O. Kim, L. Yoo, J. Sim, H.-J. Ko, K.-H. Cho, J. Kim, *Smart Mater. Struct.* 23 (2014) 1.
- [48] H. Liu, K.H. Koh, C. Lee, *Appl. Phys. Lett.* 104 (2014) 1.
- [49] H. Liu, C. Hou, J. Lin, Y. Li, Q. Shi, T. Chen, L. Sun, C. Lee, *Appl. Phys. Lett.* 113 (2018) 20.
- [50] M.-L. Seol, S.-B. Jeon, J.-W. Han, Y.-K. Choi, *Nano Energy* 31 (2017) 233.
- [51] S. Wang, Z.L. Wang, Y. Yang, *Adv. Mater.* 28 (2016) 2881.
- [52] B. Zhang, J. Chen, L. Jin, W. Deng, L. Zhang, H. Zhang, M. Zhu, W. Yang, Z.L. Wang, *ACS Nano* 10 (2016) 6241.
- [53] M. Han, X.-S. Zhang, X. Sun, B. Meng, W. Liu, H. Zhang, *Sci. Rep.* 4 (2014) 4811.
- [54] X. Li, Z.-H. Lin, G. Cheng, X. Wen, Y. Liu, S. Niu, Z.L. Wang, *ACS Nano* 8 (2014) 10674.
- [55] Y. Zi, L. Lin, J. Wang, S. Wang, J. Chen, X. Fan, P.-K. Yang, F. Yi, Z.L. Wang, *Adv. Mater.* 27 (2015) 1.



**Kah How Koh** received his B.Eng. (Hons.) degree from the Department of Electrical and Computer Engineering at the National University of Singapore. He went on to complete his Ph.D. studies in the same department under the Singapore Economic Development Board-GlobalFoundries Graduate Scholarship. After graduation, he was with the Quality Department at GlobalFoundries as a Principal Engineer, driving process improvement using methodologies and tools such as Lean Six Sigma, FMEA and SPC. He is currently a Lecturer at School of Engineering, Republic Polytechnic, Singapore. His research interests include self-powered sensors, optical MEMS and photonics for IoT applications.



**Hou Yang Tan** is currently pursuing his Diploma in Electrical and Electronic Engineering, Republic Polytechnic, Singapore. His research interests are nanotechnology, energy harvesting and Internet-of-Things.



**Qiongfeng Shi** received his B.Eng. degree from the Department of Electronic Engineering and Information Science, University of Science and Technology of China (USTC) in 2012, and received his Ph.D. degree from the Department of Electrical and Computer Engineering, National University of Singapore (NUS) in 2018. He is currently a Research Fellow in the Department of Electrical and Computer Engineering, National University of Singapore. His research interests include energy harvesters, triboelectric nanogenerator, self-powered sensors, and wearable/implantable electronics.



**Zhenwei Guo** is currently pursuing his Diploma in Electrical and Electronic Engineering in Republic Polytechnic, Singapore. His research interests include energy harvesters and artificial intelligence.



**Sen Cao** is currently pursuing his Diploma in Electrical and Electronic Engineering in Republic Polytechnic, Singapore and his research interests include energy harvesters, self-power sensors, artificial intelligence and GaN high electron mobility transistor (HEMT).



**Chengkuo Lee** received his M.S. degrees from the National Tsinghua University in 1991 and Rutgers University in 1993, and Ph.D. degree from the University of Tokyo in 1996. Currently he is an Associate Professor and Director of Center for Intelligent Sensors and MEMS at the National University of Singapore, Singapore. In 2001, he cofounded Asia Pacific Microsystems, Inc., where he was the Vice President. From 2006–2009, he was a senior member of the Technical Staff at the Institute of Microelectronics (IME), A\*STAR, Singapore. His research interests include MEMS, NEMS, sensors, energy harvesters, triboelectric nanogenerators, metamaterials, photonics, mid IR sensing, microfluidics and drug delivery.



**Daiqun Ma** is currently pursuing his Diploma in Electrical and Electronic Engineering in Republic Polytechnic, Singapore. His research interests include energy harvesters and Group III-Nitride-based gas sensors.